metals

MDPI

Article

Anisotropies in Elasticity, Sound Velocity, and Minimum Thermal Conductivity of Low Borides V_xB_y Compounds

Jing Yu [1,2], Yongmei Zhang [3], Yuhong Zhao [4,*] and Yue Ma [1,*]

1 School of Materials Science and Engineering, Beihang University, Beijing 100191, China; by1501107@buaa.edu.cn
2 School of Mechanical and Electrical Engineering, Shanxi Datong University, Datong 037009, China
3 School of Science, North University of China, Taiyuan 030051, China; yongmeizhang@nuc.edu.cn
4 School of Materials Science and Engineering, North University of China, Taiyuan 030051, China
* Correspondence: zhaoyuhong@nuc.edu.cn (Y.Z.); mayue@buaa.edu.cn (Y.M.); Tel.: +86-150-3517-2958 (Y.Z.); +86-186-1031-4763 (Y.M.)

Abstract: Anisotropies in the elasticity, sound velocity, and minimum thermal conductivity of low borides VB, V_5B_6, V_3B_4, and V_2B_3 are discussed using the first-principles calculations. The various elastic anisotropic indexes (A_U, A_{comp}, and A_{shear}), three-dimensional (3D) surface contours, and their planar projections among different crystallographic planes of bulk modulus, shear modulus, and Young's modulus are used to characterize elastic anisotropy. The bulk, shear, and Young's moduli all show relatively strong degrees of anisotropy. With increased B content, the degree of anisotropy of the bulk modulus increases while those of the shear modulus and Young's modulus decrease. The anisotropies of the sound velocity in the different planes show obvious differences. Meanwhile, the minimum thermal conductivity shows little dependence on crystallographic direction.

Keywords: first-principle; borides; anisotropy; sound velocity; thermal conductivity

check for updates

Citation: Yu, J.; Zhang, Y.; Zhao, Y.; Ma, Y. Anisotropies in Elasticity, Sound Velocity, and Minimum Thermal Conductivity of Low Borides V_xB_y Compounds. *Metals* **2021**, *11*, 577. https://doi.org/10.3390/met11040577

Academic Editor: Alain Latour Pasturel

Received: 7 March 2021
Accepted: 30 March 2021
Published: 1 April 2021

Publisher's Note: MDPI stays neutral with regard to jurisdictional claims in published maps and institutional affiliations.

Copyright: © 2021 by the authors. Licensee MDPI, Basel, Switzerland. This article is an open access article distributed under the terms and conditions of the Creative Commons Attribution (CC BY) license (https://creativecommons.org/licenses/by/4.0/).

1. Introduction

Superhard materials have long attracted tremendous attention for a wide range of applications, such as high-temperature applications, surface protection, and abrasive materials [1–15]. Diamond is the hardest substance, which maintains records of bulk modulus, shear modulus, and high hardness of 432 GPa, 535 GPa, and 60–150 GPa, respectively. Meanwhile, it is the material with the highest thermal conductivity, ~2000 W/m·K. However, the weak thermal stability of diamond at temperatures higher than 800 °C restricts the application in industry [3]. Therefore, the search for and design of new superhard materials with other unique properties is an important topic in the field of materials research. Previous studies of superhard materials have usually focused on short covalent materials [4–6], however, pure covalent materials show poor metallicity. The balance of high hardness and excellent metallicity is a central challenge to design superhard metals. However, great success has been achieved with the discovery of transition-metal (TM) light-element (LE) compounds [7–15]. It is generally believed that their high hardness stems from a combination of high valence-electron concentration to resist volume compression and strong covalent bonding to counteract shape deformation [7,8]. In addition, the TM-TM bonds of TM-LE compounds provide electron transporting paths in the crystals. Therefore, it is possible for TM-LE compounds to achieve high hardness and electrical (thermal) conductivity at the same time.

Transition-metal borides (TM_xB_y) with low boron content reduce the level of covalent bonding and significantly improve the degree of metallic bonding, which improves metallicity of materials, but not for high hardness due to the low resistance against the formation and propagation of dislocations. Surprisingly, the hardness over 40 GPa had

been firstly found in low borides $W_{0.5}Ta_{0.5}B$ by substituting W with Ta of WB [12]. Subsequently, Liang et al. had reported that a series of transition-metal monoborides exhibited surprisingly anomalous hardening behavior using the first-principles calculations [13]. Li et al. also reported that increasing boron content did not lead to higher hardness in boron-rich tungsten borides [11]. These exciting materials have raised great expectations to design superhard metals.

As candidates for hard materials, vanadium borides show favorable mechanical properties and are quite easily synthesized at normal temperatures and pressures [14–17]. The studies of low borides are surprisingly scarce, contrary to studies of other boron-rich vanadium borides [15,16]. Liang et al. analyzed the mechanical properties and mechanism of anomalous hardness of VB, V_5B_6, V_3B_4, and V_2B_3 [14]. Pan et al. had pointed out that the high elastic modulus and hardness of vanadium borides with low B content are determined by the bond strength and direction [17]. The anisotropy of a crystal reflects the periodicity of the atom arrangement along the different crystallographic orientations in the lattices, which results in the different physical properties of crystals along the different directions. A more detailed exploration of the anisotropic features of V_xB_y compounds with low boron content is helpful to understand superhard metal. In this paper, the anisotropies of VB, V_5B_6, V_3B_4, and V_2B_3 in mechanical properties (bulk modulus, shear modulus, and Young's modulus, sound velocity) and minimum thermal conductivity are discussed.

2. Method and Computation Details

Four different vanadium borides, including VB (space group: *Cmcm*), V_5B_6 (space group: *Cmmm*), V_3B_4 (space group: *Immm*), and V_2B_3 (space group: *Cmcm*), were considered in this paper. The primitive cell was used to complete the calculations in the present work. The first-principles method based on density functional theory was used with the Perdew–Burke–Ernzerhof form of generalized gradient approximation for the electronic exchange-correlation interaction implemented in MedeA VASP [18,19]. All calculations were completed with a cutoff energy of plane wave basis ~550 eV and Monkhorst–Pack k point meshes $\leq$0.02 Å^{-1} [20]. The tolerances of geometry optimization were set as the difference in the total energy being within 5.0×10^{-6} eV/atom with a maximum force per atom 0.01 eV/Å, a maximum stress of 0.02 GPa, and a maximum displacement of 5.0×10^{-4} Å. The elastic constants were obtained using the stress-strain method [21] with six strain steps for each optimized structure. Based on the elastic constants, the polycrystalline bulk modulus B and shear modulus G are obtained through the Voigt–Reusse–Hill (VRH) approximation [22]. Young's modulus E is given by

$$E = \frac{9BG}{3B + G} \tag{1}$$

Based on the assumption that the indentation size is correlated with the shear modulus G and the width of a formed imprint is proportional to the bulk modulus B, Chen et al. proposed a semi-empirical model to describe the Vickers hardness of materials [23]. This model has been widely used to predict the Vickers hardness of many materials and is given by

$$H_V = 2\left(\frac{G^3}{B^2}\right)^{0.585} - 3 \tag{2}$$

3. Results and Discussion

3.1. Equilibrium Structure and Stability

To estimate the structural stability, the cohesive energy (E_{coh}) and formation enthalpy (E_{eff}) are investigated.

$$E_{coh} = \frac{1}{x + y}\left(E^{total} - xE_V^{atom} - yE_B^{atom}\right) \tag{3}$$

$$E_{\text{eff}} = \frac{1}{x+y}\left(E^{\text{total}} - xE_{\text{V}}^{\text{g}} - yE_{\text{B}}^{\text{g}}\right) \quad (4)$$

where x (y) is the number of V (B) atoms in the unit cell, E^{total} is the total energy of the V_xB_y compound, $E_{\text{V}}^{\text{atom}}$ and $E_{\text{B}}^{\text{atom}}$ are the energies of the free V and B atoms, E_{V}^{g} and E_{B}^{g} are the energy per atom in its ground state. The optimized lattice constants, cohesive energy, and formation enthalpy are listed in Table 1, together with the available theoretical and experimental results. The negative cohesive energy and formation enthalpy indicate that these structures are thermodynamically stable. The stability follows the order VB > V_5B_6 > V_3B_4 > V_2B_3; the same result can also be obtained from the position of Fermi level (E_{F}) of the total density of states (see Figure 1). The structural stability of materials can be judged from the position of Fermi surface in the density of states curve [24]. The higher the value of E_{F}, the lower the stability of the structure.

Table 1. Calculated lattice constants a, b, and c (Å), cohesive energy E_{coh} (eV), and formation enthalpy E_{eff} (eV) of VB, V_5B_6, V_3B_4, and V_2B_3 with the available data for comparison.

-		VB	V_5B_6	V_3B_4	V_2B_3
	present	3.047	2.972	2.975	3.039
a	Ref. [13]	3.050	2.976	2.980	3.039
	Exp. [21]	3.100	3.058	-	3.060
	present	8.035	21.213	3.041	18.392
b	Ref. [13]	8.036	21.220	3.042	18.408
	Exp. [22]	8.170	21.250	-	18.429
	present	2.966	3.046	13.199	2.977
c	Ref. [13]	2.969	3.049	13.208	2.982
	Exp. [23]	2.980	2.974	-	2.984
E_{coh}	present	−8.517	−8.414	−8.354	−8.280
E_{eff}	present	−0.851	−0.833	−0.822	−0.801

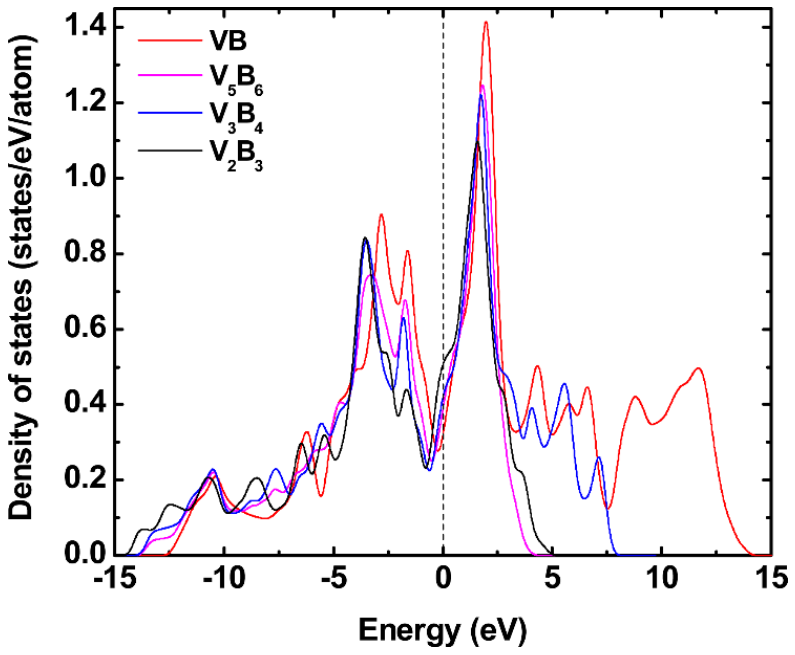


Figure 1. The total density of states with Fermi level E_{F} (vertical dashed line) of V_xB_y.

3.2. Elastic Properties

The present elastic moduli and Vickers hardness H_V data are shown in Table 2. Generally, the compressibility of solids under pressure is expressed by the bulk modulus. The greater the bulk modulus of solids, the less compressible they are. The shear modulus reflects the resistance to shape change under shear force. Young's modulus is related to the stiffness of materials. It can be seen that the bulk, shear, and Young's moduli of V_xB_y all follow the order V_2B_3 > V_3B_4 > V_5B_6 > VB. Furthermore, the values are very close to each other. Table 2 shows the theoretical Vickers hardness value of V_xB_y compounds is close to 40 GPa, indicating these V_xB_y compounds are potential superhard materials [25].

Table 2. Calculated bulk modulus B (in Gpa), shear modulus G (in Gpa), Young's modulus E (in Gpa), and Vickers hardness H_V (in GPa) of V_xB_y.

-	VB	V_5B_6	V_3B_4	V_2B_3
B	266.5	272.8	276	279.2
G	235.5	237.7	237.9	242.4
E	545.7	552.5	554.4	564
H_V	39.3	38.8	38.3	39.1

3.3. Elastic Anisotropy

Elastic anisotropy has great research value for ceramics due to its correlation with the generation of microcracks and lattice deformation [26,27]. The orientation dependence of three-dimensional (3D) elastic moduli are typically used to describe the elastic anisotropy of a crystal. Considering the effects of shear surface and direction on shear modulus, the average shear modulus over all possible directions is calculated. The formulae of bulk modulus, shear modulus, and Young's modulus of an orthorhombic structure can be obtained from the direction cosines (l_1, l_2, and l_3) and elastic compliance constant S_{ij} [28], and are given by

$$\frac{1}{B} = (S_{11} + S_{12} + S_{13})l_1^2 + (S_{12} + S_{22} + S_{23})l_2^2 + (S_{13} + S_{23} + S_{33})l_3^2 \quad (5)$$

$$\begin{aligned}\frac{1}{G} = {} & 2l_1^2(1 - l_1^2)S_{11} + 2l_2^2(1 - l_2^2)S_{22} + 2l_3(1 - l_3^2)S_{33} - 4l_1^2l_2^2S_{12} - 4l_1^2l_3^2S_{13} - 4l_2^2l_3^2S_{23} \\ & + \tfrac{1}{2}(1 - l_1^2 - 4l_2^2l_3^2)S_{44} + \tfrac{1}{2}(1 - l_2^2 - 4l_1^2l_3^2)S_{55} + \tfrac{1}{2}(1 - l_3^2 - 4l_1^2l_2^2)S_{66}\end{aligned} \quad (6)$$

$$\frac{1}{E} = l_1^4S_{11} + l_2^4S_{22} + l_3^4S_{33} + 2l_1^2l_2^2S_{12} + 2l_1^2l_3^2S_{13} + 2l_2^2l_3^2S_{23} + l_2^2l_3^2S_{44} + l_1^2l_3^2S_{55} + l_1^2l_2^2S_{66} \quad (7)$$

Figure 2 shows the 3D surface contours and their projections in different planes of the bulk modulus. In this context, a 3D plot is spherical for an isotropic material, and the deviation from a sphere describes the degree of anisotropy. The ellipsoids of the 3D bulk modulus of four structures indicate relatively strong anisotropy in linear compressibility. Furthermore, the 3D contours of VB and V_2B_3 are similar. The shrinking of the 3D plot depicted in blue indicates the small linear incompressibility along that direction. Based on the ratio of maximum to minimum of directional bulk modulus B_{max}/B_{min}, the order of anisotropy in the bulk modulus is VB < V_5B_6 < V_3B_4 < V_2B_3. In their planar projections, the nearly circular shape of VB and V_2B_3 in (100) plane is due to the approximately equal values of C_{22} and C_{33}. The larger distorted shapes in the (010) and (001) planes indicate its strong anisotropy in linear compressibility. For V_5B_6, the similar anisotropy is observed due to the coincident profiles in the (100) and (010) planes, while the anisotropy of the linear compressibility in the (001) plane is very weak due to the small difference of C_{11} and C_{22}. The anisotropies of the linear compressibility in the (100) and (001) planes are also similar for V_3B_4, while that in the (010) plane is also very weak.

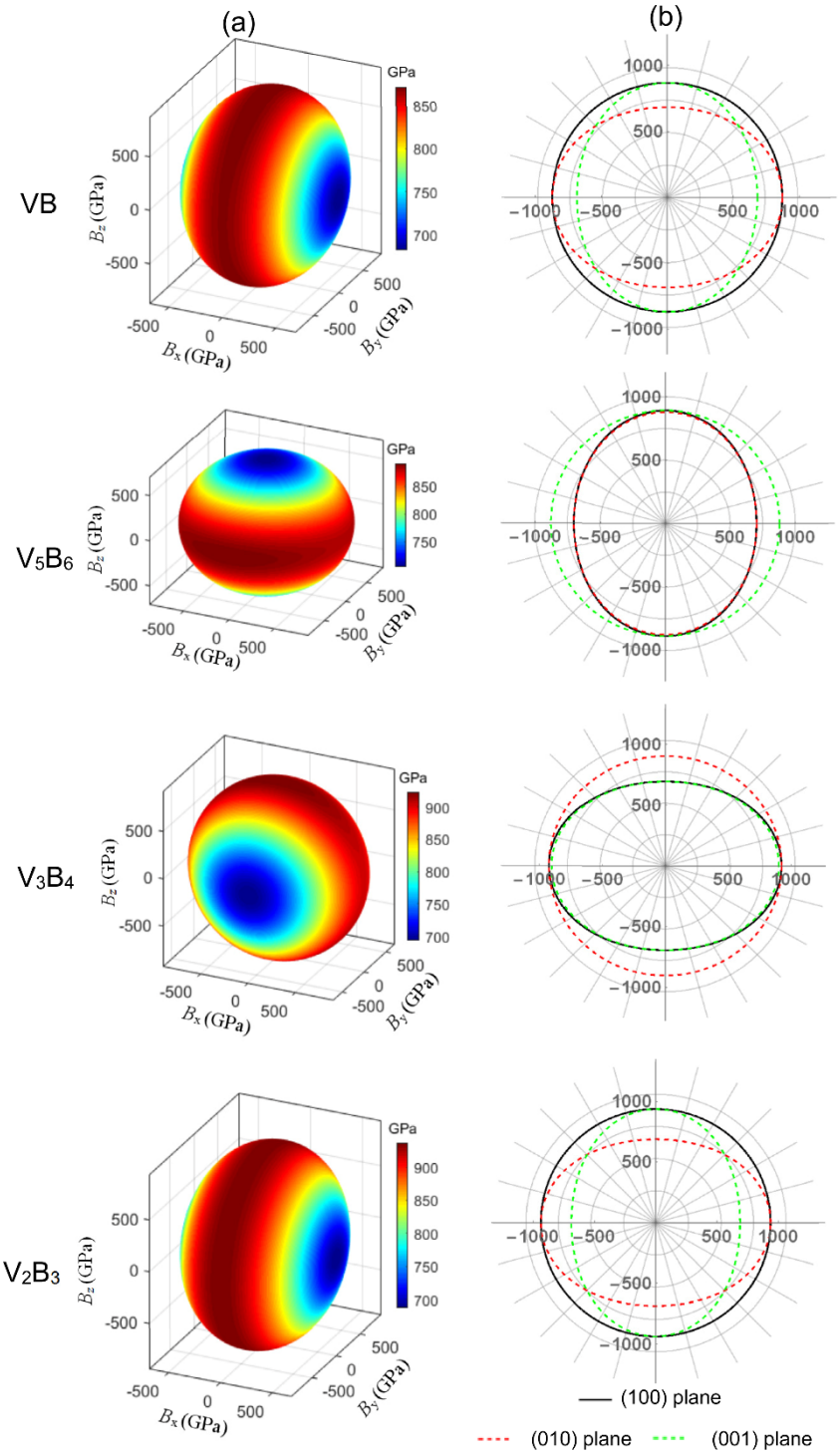


Figure 2. (**a**) Orientation dependence of bulk modulus and (**b**) planar projections in (100), (010), and (001) planes of V_xB_y.

Figure 3 shows the 3D surface contours and their projections of shear modulus in different planes. The strongly curved surface shapes suggest strong anisotropy in the shear modulus. Based on the ratio of the maximum to minimum value of the directional shear modulus G_{max}/G_{min}, the order of anisotropy in the shear modulus is VB > V_5B_6 > V_3B_4 > V_2B_3. For VB, the shear moduli in all planes show relatively strong anisotropy. However, the weakest anisotropy is found in the (100) plane for V_5B_6 with G_{max}/G_{min}~1.096, in the (100) and

(010) planes for V_3B_4 with G_{max}/G_{min}~1.095 and ~1.097, and in the (100) and (001) planes for V_2B_3 with G_{max}/G_{min}~1.056 and ~1.044, respectively.

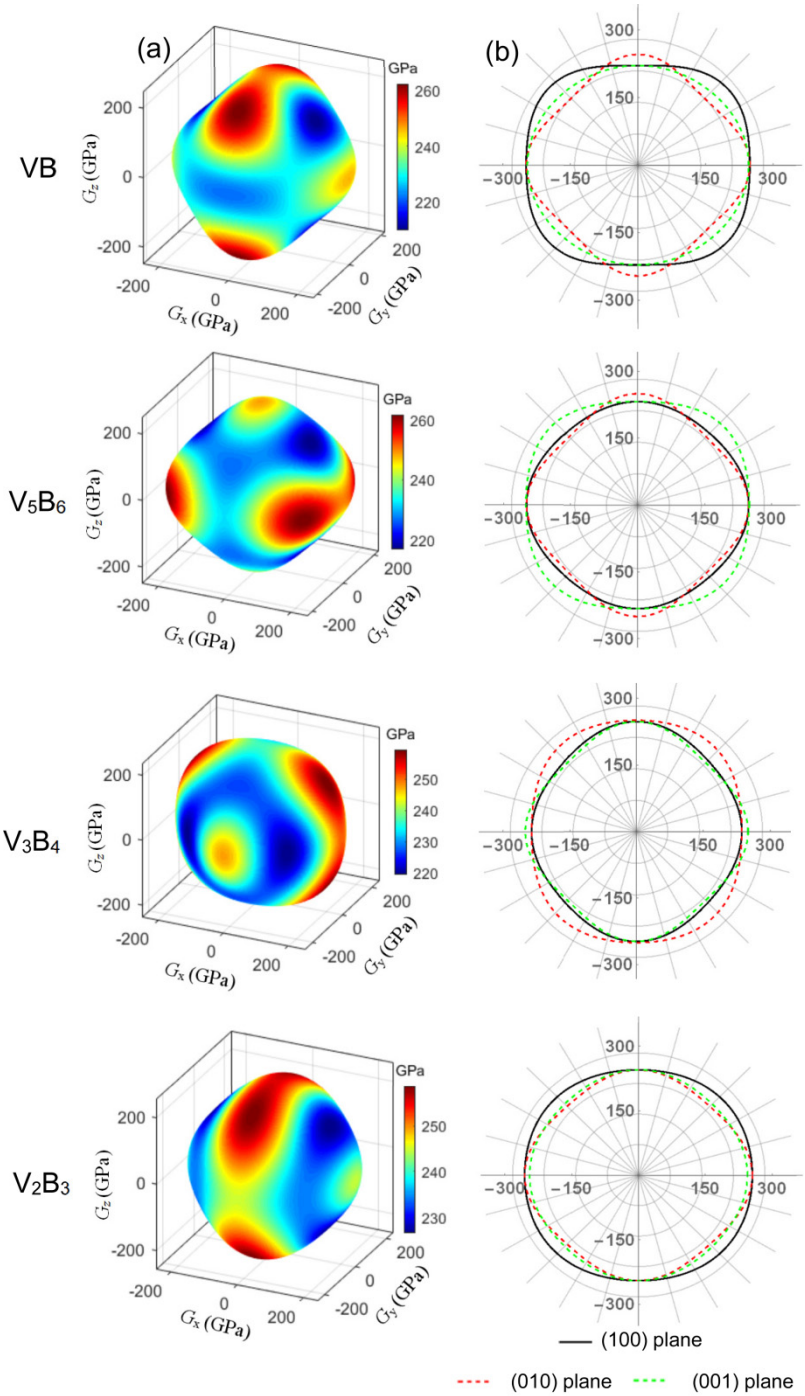


Figure 3. (**a**) Orientation dependence of shear modulus and (**b**) planar projections in (100), (010), and (001) planes of V_xB_y.

Similarly, the 3D surface contours of the Young's modulus shown in Figure 4 are also distorted, suggesting the strongly anisotropic feature. According to the ratio of maximum to minimum of directional Young's modulus E_{max}/E_{min}, the order of anisotropy in the Young's modulus is VB > V_5B_6 > V_3B_4 > V_2B_3. The projections of the Young's modulus in the different planes indicate relatively strong anisotropy, except in the (010) plane for V_3B_4 with E_{max}/E_{min}~1.084 and in the (001) plane for V_2B_3 with E_{max}/E_{min}~1.048. The anisotropy of the Young's modulus reflects a change of strength of the chemical bonds.

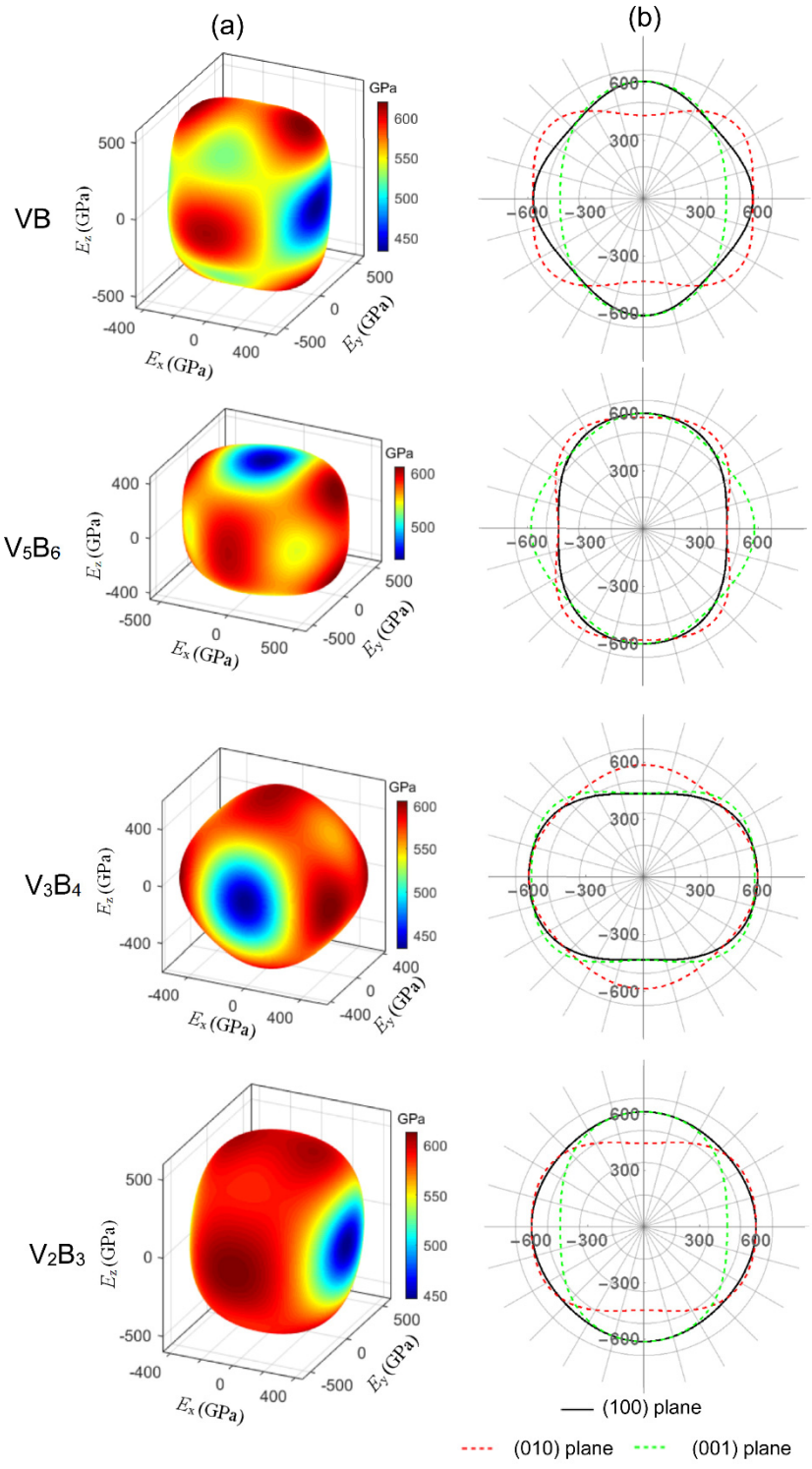


Figure 4. (**a**) Orientation dependence of Young's modulus and (**b**) planar projections in (100), (010), and (001) planes of V_xB_y.

The elastic anisotropy can be estimated by the universal elastic anisotropic index $A_U = 5\frac{G_V}{G_R} + \frac{B_V}{B_R} - 6$ (where B_V (G_V) and B_R (G_R) are the bulk (shear) modulus in Voigt and Reuss approximations) [29] and percent anisotropy in compression $A_{comp} = \frac{B_V - B_R}{B_V + B_R}$ and shear $A_{shear} = \frac{G_V - G_R}{G_V + G_R}$ [30], respectively. For an elastic isotropic crystal, $A_U = A_{comp} = A_{shear} = 0$ [29,30]. A larger deviation degree from zero means a stronger anisotropy.

Figure 5 gives the variation trends of various elastic anisotropic indexes and the ratios of B_{max}/B_{min}, G_{max}/G_{min}, and E_{max}/E_{min} of V_xB_y. It is obvious that the variation trends of the anisotropy in A_{comp}, A_{shear}, and A_U agree well with the results obtained from 3D surface contours of the bulk, shear, and Young's modulus. The compression anisotropy increases, while the shear anisotropy decreases with the increased content of B atoms. The universal elastic anisotropic index includes the contributions of polycrystalline shear and bulk modulus [31]. The elastic anisotropy is mainly determined by the shear anisotropy due to the similar variation tendency between A_{shear} and A_U. According to the values A_U and E_{max}/E_{min}, the order of elastic anisotropy is VB > V_5B_6 > V_3B_4 > V_2B_3.

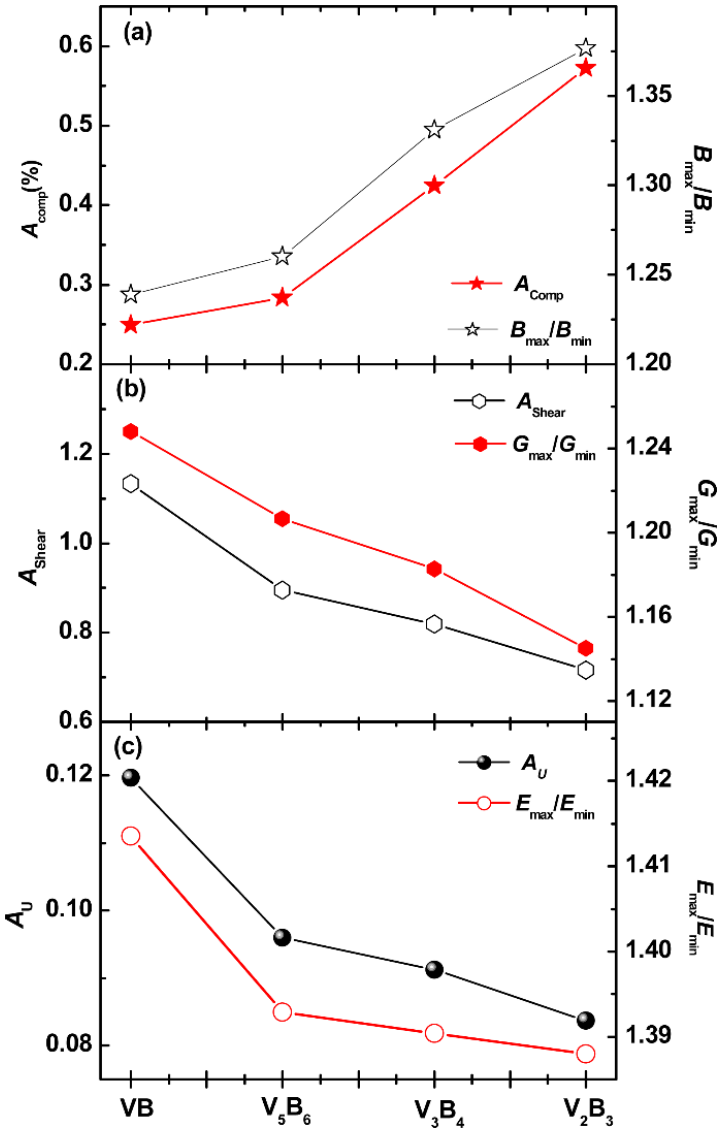


Figure 5. (**a**–**c**) Variation trends of elastic anisotropic indexes of V_xB_y. For comparison, the ratios of B_{max}/B_{min}, G_{max}/G_{min}, and E_{max}/E_{min} are also plotted.

3.4. Anisotropy in Sound Velocity

Based on the classic theory of transportation of phonon gas solid, the sound velocity of a crystal structure can be employed to estimate the thermal conductivity [32]. In a specific crystallographic plane, the sound velocity consists of three orthogonal modes, a

pure transverse mode v_t and two mixed modes $v_\pm$, by solving the Christoffel equation [33]. The three modes of velocity are given by

$$\rho v_t^2 = a_1 \sin^2\theta_k + a_2 \cos^2\theta_k \quad (8)$$

$$2\rho v_\pm^2 = a_3 \sin^2\theta_k + a_4 \cos^2\theta_k \pm \left[\left(a_5 \sin^2\theta_k - a_6 \cos^2\theta_k\right)^2 + (2a_7 \sin\theta_k \cos\theta_k)^2\right]^{1/2} \quad (9)$$

where the values of a_i can be obtained using the elastic constants, and θ_k is the angle of wave vector k with respect to one of the symmetry axes.

The projections of sound velocity (v_t and $v_\pm$) in the different crystallographic planes for V_xB_y are plotted in Figure 6. Table 3 gives the ratio of maximum to minimum of sound velocity of V_xB_y. It can be seen that the faster mode v_+ is larger than pure transverse mode v_t and slow mode v_-, and the values of v_t and v_- are comparable. The profiles of three acoustic branches (v_t and $v_\pm$) of four structures are different in (100), (010), and (001) planes. The ratio of maximum to minimum of sound velocity in different planes (Table 3) indicates the degree of anisotropy. The anisotropies in v_t of V_5B_6, V_3B_4, and V_2B_3 are relatively weak at (100), (010), and (001) planes, which is mainly determined by the small difference of elastic constants C_{44}, C_{55}, C_{66}. The degree of anisotropy of two mixed modes is determined by the diagonal and off-diagonal elements of the elastic constant matrix.

Table 3. Ratio of maximum to minimum of sound velocity (v_t and $v_\pm$, km/s) in the different crystallographic planes of V_xB_y.

-		VB	V_5B_6	V_3B_4	V_2B_3
v_t	(100) plane	1.129	1.075	1.050	1.041
	(010) plane	1.009	1.005	1.061	1.044
	(001) plane	1.119	1.081	1.011	1.003
v_+	(100) plane	1.057	1.142	1.151	1.019
	(010) plane	1.143	1.139	1.031	1.147
	(001) plane	1.146	1.041	1.144	1.158
v_-	(100) plane	1.110	1.043	1.058	1.032
	(010) plane	1.179	1.145	1.063	1.098
	(001) plane	1.004	1.084	1.130	1.043

3.5. Anisotropy in Minimum Thermal Conductivity

The minimum thermal conductivity is an important parameter for high-temperature applications of materials, which can be evaluated via the Cahill model [34]. The obtained three sound modes (v_t and $v_\pm$) by solving the Christoffel equation are also used.

$$\kappa_{\min} = \frac{k_B}{2.48}\left(\frac{n}{V}\right)^{2/3}(v_t + v_+ + v_-) \quad (10)$$

Here, k_B is Boltzmann's constant, n is the number of atoms per molecule, and V is the volume per molecule. The unit of $\kappa_{\min}$ is W/(m·K). Figure 7 gives the planar projections of minimum thermal conductivity in (100), (010), and (001) crystallographic planes for V_xB_y. It can be found that the differences in profiles of minimum thermal conductivities in different planes are small. Furthermore, these curves show little dependence on crystallographic direction, indicating the anisotropy of minimum thermal conductivity is very weak, which also can be obtained from the ratio of maximum to minimum of minimum thermal conductivity in the different crystallographic planes (Table 4). Based on the Callaway–Debye theory, the minimum thermal conductivity is correlated to the Debye temperature [35]. Thus, the anisotropic feature of minimum thermal conductivity also reflects the anisotropy of the Debye temperature.

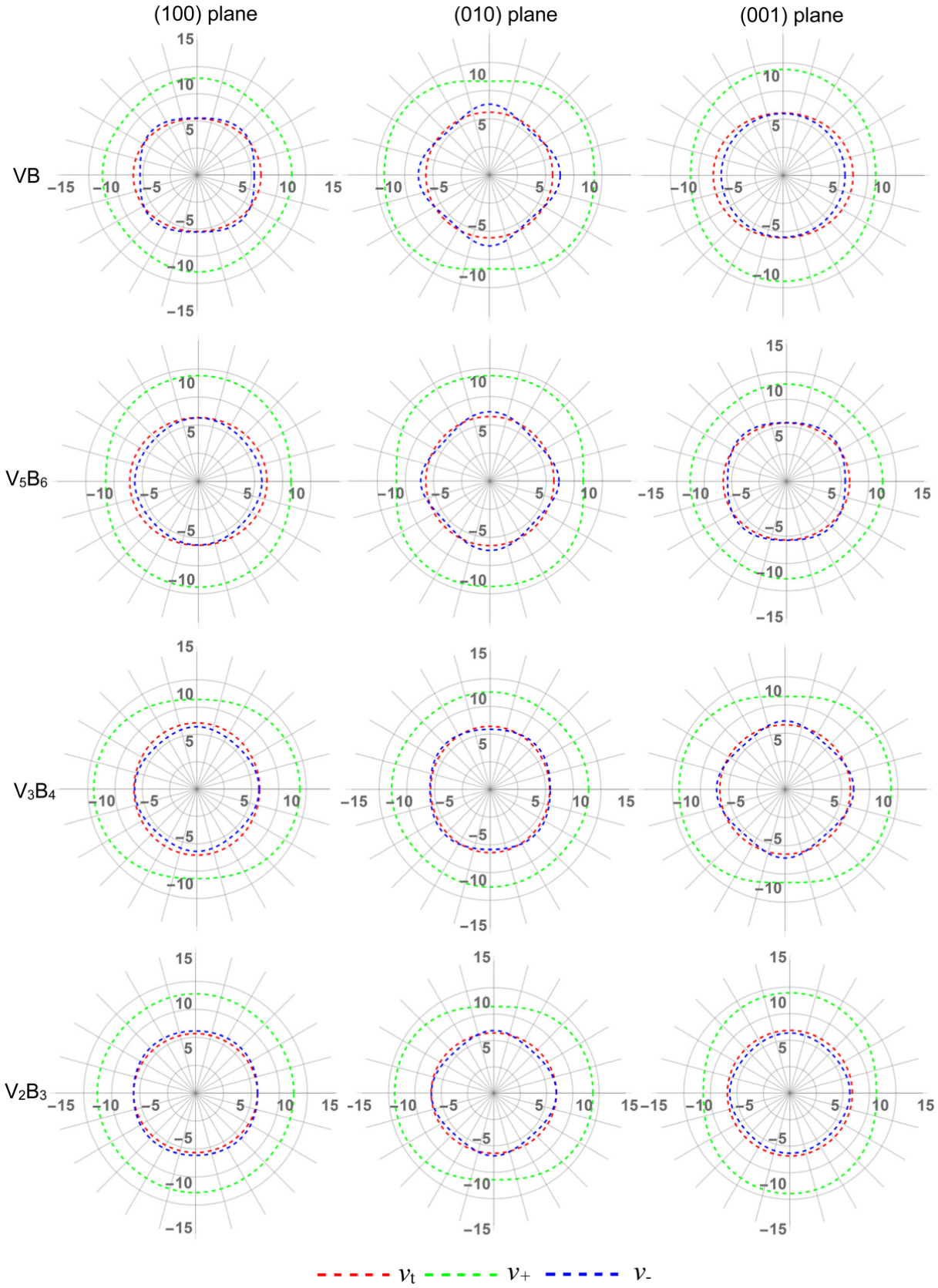


Figure 6. Anisotropies of sound velocity (v_t and $v_\pm$) in (100), (010), and (001) planes for V_xB_y.

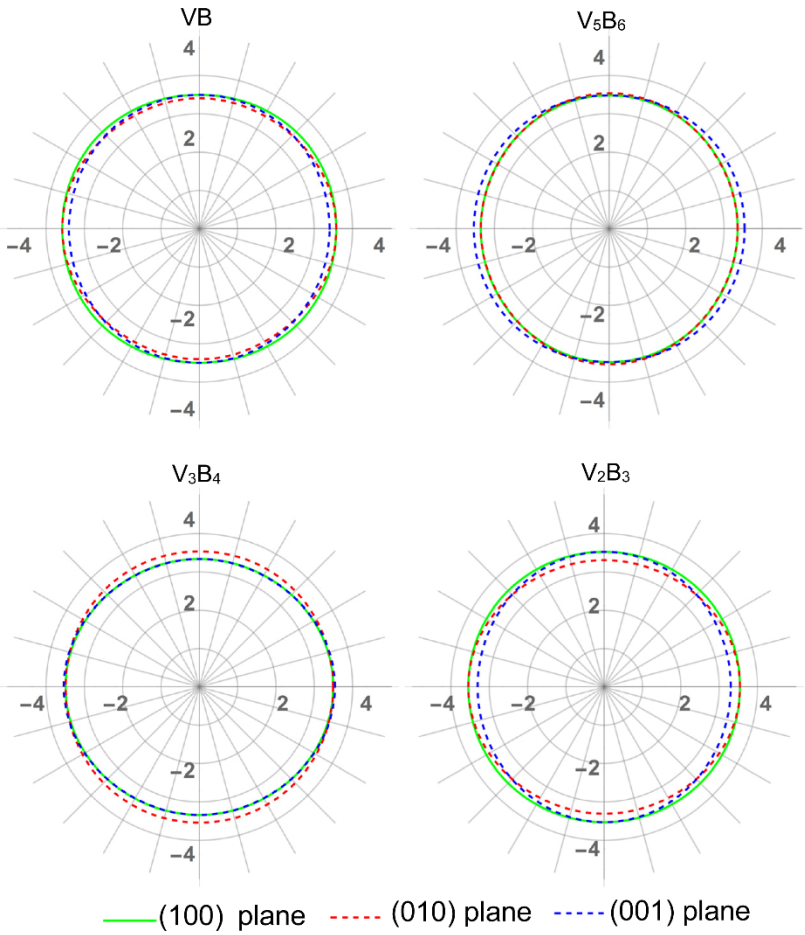


Figure 7. Anisotropies of minimum thermal conductivity in the (100), (010), and (001) planes for V_xB_y.

Table 4. Ratio of maximum to minimum of minimum thermal conductivity in the different crystallographic planes of V_xB_y.

-		VB	V_5B_6	V_3B_4	V_2B_3
κ_{min}	(100) plane	1.027	1.037	1.048	1.007
	(010) plane	1.053	1.054	1.014	1.073
	(001) plane	1.027	1.019	1.060	1.066

4. Conclusions

The first-principles method is used to investigate the stability, anisotropies in elasticity, sound velocity, and minimum thermal conductivity of low borides VB, V_5B_6, V_3B_4, and V_2B_3. All compounds are thermodynamically stable. The stability follows the order VB > V_5B_6 > V_3B_4 > V_2B_3. The calculated Vickers hardness of VB, V_5B_6, V_3B_4, and V_2B_3 are close to 40 GPa, indicating that these V_xB_y compounds are potential superhard materials. The elastic anisotropic indexes (A_U, A_{comp}, and A_{shear}), 3D surface contours, and their planar projections in different crystallographic planes of bulk, shear, and Young's moduli are used to characterize the elastic anisotropy. All V_xB_y compounds show a relatively strong elastic anisotropic feature, which is mainly determined by the shear anisotropy. The order of elastic anisotropy is VB > V_5B_6 > V_3B_4 > V_2B_3. The anisotropies of sound velocity in different crystallographic planes show obvious differences. The minimum thermal conductivities for all V_xB_y compounds in different planes are comparable and show very weak anisotropy.

Author Contributions: J.Y.: Conceptualization, Software, Data curation, Writing—Original draft preparation, Formal analysis; Y.Z. (Yongmei Zhang): Methodology; Y.Z. (Yuhong Zhao): Software, Validation; Y.M.: Writing—Reviewing and Editing, Project administration. All authors have read and agreed to the published version of the manuscript.

Funding: This research received no external funding.

Institutional Review Board Statement: Not applicable.

Informed Consent Statement: Not applicable.

Data Availability Statement: The data presented in this study are available on request from the corresponding authors.

Conflicts of Interest: The authors declare no conflict of interest.

References

1. Kaner, R.B.; Gilma, J.J.; Tolbert, S.H. Designing superhard materials. *Science* **2005**, *308*, 1268–1269. [CrossRef]
2. Burrage, K.C.; Lin, C.M.; Chen, W.C.; Chen, C.C.; Vohra, Y.K. Experimental and computational studies on superhard material rhenium diboride under ultrahigh pressures. *Materials* **2020**, *13*, 1657. [CrossRef] [PubMed]
3. Joha, P.; Polwart, N.; Troupe, C.E.; Wilson, J.I.B. The oxidation of (100) textured diamond, Diamond. *Relat. Mater.* **2002**, *11*, 861.
4. Dub, S.; Lytvyn, P.; Strelchuk, V.; Nikolenko, A.; Stubrov, Y.; Petrusha, I.; Taniguchi, T.; Ivakhnenko, S. Vickers hardness of diamond and CBN single crystals: AFM approach. *Crystals* **2017**, *7*, 369. [CrossRef]
5. Lonsdale, K. Further comments on attempts by H. Moissan, J.B. Hannay and Sir Charles Parsons to make diamonds in the laboratory. *Nature* **1962**, *196*, 104–106. [CrossRef]
6. Mohammadi, R.; Xie, M.; Lech, A.T.; Turner, C.L.; Kavner, A.; Tolbert, S.H.; Kaner, R.B. Toward inexpensive superhard materials, Tungsten tetraboride-based solid solutions. *J. Am. Chem. Soc.* **2012**, *134*, 20660–20668. [CrossRef]
7. Chung, H.Y.; Weinberger, M.B.; Levine, J.B.; Kavner, A.; Yang, J.M.; Tolbert, S.H.; Kaner, R.B. Synthesis of ultra-incompressible superhard rhenium diboride at ambient pressure. *Science* **2007**, *316*, 436–439. [CrossRef]
8. Akopov, G.; Pangilinan, L.E.; Mohammadi, R.; Kaner, R.B. Perspective: Superhard metal borides: A look forward. *APL Mater.* **2018**, *6*, 070901. [CrossRef]
9. Akopov, G.; Yeung, M.T.; Kaner, R.B. Rediscovering the Crystal Chemistry of Borides. *J. Adv. Mater.* **2017**, *29*, 1604506. [CrossRef]
10. Yeung, M.T.; Mohammadi, R.; Kaner, R.B. Ultraincompressible, superhard materials. *Annu. Rev. Mater. Res.* **2016**, *46*, 465–485. [CrossRef]
11. Li, Q.; Zhou, D.; Zheng, W.; Ma, Y.; Chen, C. Anomalous Stress Response of Ultrahard WB_n Compounds. *Phys. Rev. Lett.* **2015**, *115*, 185502. [CrossRef] [PubMed]
12. Yeung, M.T.; Lei, J.; Mohammadi, R.; Turner, C.L.; Wang, Y.; Tolbert, S.H.; Kaner, R.B. Superhard Monoborides: Hardness Enhancement through Alloying in $W_{1-x}Ta_xB$. *Adv. Mater.* **2016**, *28*, 6993–6998. [CrossRef] [PubMed]
13. Liang, Y.; Gao, Z.; Qin, P.; Gao, L.; Tang, C. The mechanism of anomalous hardening in transition-metal monoborides. *Nanoscale* **2017**, *9*, 9112–9118. [CrossRef]
14. Liang, Y.; Qin, P.; Jiang, H.; Zhang, L.; Zhang, J.; Tang, C. Designing superhard metals: The case of low borides. *AIP Adv.* **2018**, *8*, 045305. [CrossRef]
15. Wei, S.L.; Li, D.; Lv, Y.Z.; Liu, Z.; Tian, F.B.; Duan, D.F.; Liu, B.B.; Cui, T. Strong covalent boron bonding induced extreme hardness of VB_3. *J. Alloys Compd.* **2016**, *688*, 1101–1107. [CrossRef]
16. Wu, L.; Wan, B.; Zhao, Y.; Zhang, Y.; Liu, H.; Wang, Y.; Zhang, J.; Gou, H. Unraveling stable vanadium tetraboride and triboride by first-principles computations. *J. Phys. Chem. C.* **2015**, *119*, 21649–21657. [CrossRef]
17. Pan, Y.; Lin, Y.H.; Guo, J.M.; Wen, M. Correlation between hardness and bond orientation of vanadium borides. *RSC Adv.* **2014**, *4*, 47377. [CrossRef]
18. Perdew, J.P.; Burke, K.; Ernzerho, M.F. Generalized Gradient Approximation Made Simple. *Phys. Rev. Lett.* **1996**, *77*, 3865. [CrossRef]
19. Kresse, G.; Furthmuller, J. Efficient iterative schemes for ab initio total-energy calculations using a plane-wave basis set. *Phys. Rev. B* **1996**, *54*, 11169. [CrossRef]
20. Monkhorst, H.J.; Pack, J.D. Special points for Brillouin-zone integrations. *Phys. Rev. B* **1976**, *13*, 5188–5192. [CrossRef]
21. Fan, C.Z.; Zeng, S.Y.; Li, L.X.; Zhan, Z.J.; Liu, R.P.; Wang, W.K.; Zhang, P.; Yao, Y.G. Potential superhard osmium dinitride with fluorite and pyrite structure: First-principles calculations. *Phys. Rev. B* **2006**, *74*, 125118. [CrossRef]
22. Hill, R. The elastic behaviour of a crystalline aggregate. *Proc. Phys. Soc. A* **1952**, *65*, 349–354. [CrossRef]
23. Chen, X.Q.; Niu, H.; Li, D.; Li, Y. Modeling hardness of polycrystalline materials and bulk metallic glasses. *Intermetallics* **2011**, *19*, 1275. [CrossRef]
24. Du, J.L.; Wen, B.; Melnik, R.; Kawazoe, Y. First-principles studies on structural, mechanical, thermodynamic and electronic properties of NieZr intermetallic compounds. *Intermetallics* **2014**, *54*, 110–119. [CrossRef]
25. Solozhenko, V.L.; Gregoryanz, E. Synthesis of superhard materials. *Mater. Today* **2005**, *8*, 44–51. [CrossRef]

26. Kong, Z.; Peng, M.; Sun, Y.; Qu, D.; Bao, L. Theoretical predictions of elastic anisotropies and thermal properties of $TMRe_2$ (TM = Sc, Y, Zr and Hf). *Phys. B Condens. Matter* **2019**, *571*, 222. [CrossRef]
27. Qu, D.; Bao, L.; Kong, Z.; Duan, Y. Anisotropy of elastic and thermal properties of $TMOs_2$(TM = Sc, Y, Ti, Zr and Hf) from first-principles explorations. *Mater. Res. Express* **2019**, *6*, 116569. [CrossRef]
28. Zhang, M.G.; Yan, H.Y. Elastic anisotropy and thermodynamic properties of iron tetraboride under high pressure and high temperature. *Solid State Commun.* **2014**, *187*, 53–58. [CrossRef]
29. Ranganathan, S.I.; Ostoja-Starzewski, M. Universal elastic anisotropy index. *Phys. Rev. Lett.* **2008**, *101*, 055504–055507. [CrossRef]
30. Chung, D.H.; Buessem, W.R. The elastic anisotropy of crystals. *J. Appl. Phys.* **1967**, *38*, 2010–2012. [CrossRef]
31. Zhang, Y.M.; Liu, D.; Shi, Y.D.; Sun, Z.Y.; Wu, L.; Gao, Y.Q. Elastic anisotropy and physical properties of semi-transition-metal borides: First- principles calculation. *Appl. Phys. Express* **2020**, *13*, 015501. [CrossRef]
32. Feng, J.; Xiao, B.; Zhou, R.; Pan, W. Anisotropy in elasticity and thermal conductivity of monazite-type REPO4 (RE = La, Ce, Nd, Sm, Eu and Gd) from first-principles calculations. *Acta Mater.* **2013**, *61*, 7364–7383. [CrossRef]
33. Lau, K.; McCurdy, A.K. Elastic anisotropy factor fot orthorhomic, tetragonal, and hexagonal crystals. *Phys. Rev. B* **1998**, *58*, 8980. [CrossRef]
34. Cahill, D.G.; Watson, S.K.; Pohl, R.O. Lower limit to the thermal conductivity of disordered crystals. *Phys. Rev. B* **1992**, *46*, 6131. [CrossRef] [PubMed]
35. Luo, Y.; Wang, J.; Li, J.; Hu, Z.; Wang, J. Theoretical study on crystal structures, elastic stiffness, and intrinsic thermal conductivities of β-, γ-, and δ-$Y_2Si_2O_7$. *J. Mater. Res.* **2015**, *30*, 493. [CrossRef]